IVYSPRING INTERNATIONAL PUBLISHER

Theranostics

2022; 12(1): 59-75. doi: 10.7150/thno.64862

Research Paper

A hydrogen peroxide economizer for on-demand oxygen production-assisted robust sonodynamic immunotherapy

Qinqin Jiang[1*], Bin Qiao[1*], Xiaohong Lin[1], Jin Cao[1], Nan Zhang[2], Huanling Guo[2], Weiwei Liu[1], Lingyu Zhu[3], Xue Xie[1], Li Wan[1], Rui Tang[1], Bing Liang[4], Dong Wang[5], Zhigang Wang[1], Yang Zhou[6], HaiTao Ran[1], Pan Li[1]✉

1. Department of Ultrasound, Chongqing Key Laboratory of Ultrasound Molecular Imaging, the Second Affiliated Hospital of Chongqing Medical University, Chongqing 400010, P. R. China.
2. Department of Medical Ultrasonics, The First Affiliated Hospital of Sun Yat-sen University, Guangzhou, 510080, P. R. China.
3. Department of Ultrasound China-Japan Union Hospital of Jilin University, Jilin 130033, P. R. China.
4. Department of Pathology, Chongqing Medical University, Chongqing, 400016, P. R. China.
5. Department of Ultrasound, the First Affiliated Hospital of Chongqing Medical University, Chongqing 400010, China.
6. Department of Ultrasound, the Third People's Hospital of Chengdu City, the Affiliated Hospital of Southwest Jiaotong University.

*Qinqin Jiang and Bin Qiao are co-first authors who contributed equally to this work.

✉ Corresponding author: Pan Li, E-mail: lipan@hospital.cqmu.edu.cn.

Received: 2021.07.12; Accepted: 2021.10.12; Published: 2022.01.01

Abstract

The outcome of sonodynamic immunotherapy is significantly limited by tumor hypoxia. To overcome this obstacle, one common solution is to catalyze the conversion of endogenous H_2O_2 into O_2. However, the effectiveness of this strategy is limited by the insufficient concentration of H_2O_2 in the tumor microenvironment (TME). Herein, we developed a H_2O_2 economizer for on-demand O_2 supply and sonosensitizer-mediated reactive oxygen species production during ultrasound activation, thereby alleviating hypoxia-associated limitations and augmenting the efficacy of sonodynamic immunotherapy.

Methods: The H_2O_2 economizer is constructed by electrostatic adsorption and π–π interactions between the Fe-doped polydiaminopyridine (Fe-PDAP) nanozyme and chlorin e6. By employing a biomimetic engineering strategy with cancer cell membranes, we addressed the premature leakage issue and increased tumor-site accumulation of nanoparticles (membrane-coated Fe-PDAP/Ce6, MFC).

Results: The prepared MFC could significantly attenuate the catalytic activity of Fe-PDAP by reducing their contact with H_2O_2. Ultrasound irradiation promoted MFC dissociation and the exposure of Fe-PDAP for a more robust O_2 supply. Moreover, the combination of MFC-enhanced sonodynamic therapy with anti-programmed cell death protein-1 antibody (aPD-1) immune checkpoint blockade induced a strong antitumor response against both primary tumors and distant tumors.

Conclusion: This as-prepared H_2O_2 economizer significantly alleviates tumor hypoxia via reducing H_2O_2 expenditure and that on-demand oxygen-elevated sonodynamic immunotherapy can effectively combat tumors.

Key words: sonodynamic therapy, immunotherapy, nanozyme, cancer cell membrane, focused ultrasound

Introduction

Sonodynamic therapy (SDT) emerges as a promising site-specific tumor cells killing strategy due to the unique features with non-invasiveness, great operational feasibility, and high tissue penetration depth. It uses low-intensity ultrasound (US) as a source of stimuli to generate highly cytotoxic reactive oxygen species (ROS) *via* activation of a sonosensitizer [1-4]. Recently, it has been found that SDT can release

tumor-associated antigens (TAAs) and induce immunogenic cell death (ICD), which facilitate the redistribution and activation of immune effector cells with enhanced tumor-specific T cell infiltration. The combination of checkpoint blockade with SDT has shown a synergistic effect on tumor treatment.[1] Unfortunately, such a sonodynamic immunotherapy approach is not strong enough to eliminate tumors because the highly hypoxic tumor microenvironment (TME) makes it difficult to generate robust ROS during cancer treatment, giving rise to insufficient TAAs generation and limited antitumor immune effect.[5-7] Therefore, there is a pressing need to explore practical strategies for elevating the tumor oxygen content while simultaneously enhancing the benefit of sonodynamic immunotherapy.

Recently, various oxygen carriers, such as hemoglobin and perfluorocarbons, have been explored for their ability to elevate the tumor oxygen content.[8-10] However, the outcomes are limited by low O_2-loading efficiency. Alternatively, *in situ* catalysis of O_2 generation inside tumors is a common oxygen-replenishing strategy [11-13]. To this end, several O_2-releasing nanosystems (*e.g.*, manganese dioxide nanoparticles, gold nanoclusters, and Fe^{3+}-doped building blocks) have been reported [14-18]; these nanosystems can be transported to tumor sites and catalyze the conversion of endogenous H_2O_2 into O_2. However, these strategies suffer from insufficient concentrations of H_2O_2 (50-100 μM) in the TME, and their outcomes are limited.[19, 20] In addition, the O_2-evolving catalytic reaction process is usually rapid and uncontrolled. The inevitable premature consumption of H_2O_2 by catalase could lead to insufficient H_2O_2 supply during O_2-augmented SDT, which prevents alleviation of hypoxia-related SDT resistance during the therapeutic process. Therefore, solutions that allow "broadening sources" of H_2O_2 in the TME are highly desirable for efficient O_2 generation and hypoxia alleviation, which has been rarely reported.

We assume that the surface carrying agents on catalase could significantly lock the catalase-like activity due to the reduced contact with H_2O_2 [21, 22]. Upon ultrasound irradiation, the carrying agents disintegrate from the catalase *via* the cavitation effect, and their catalytic capability is recovered [23-27]. On this basis, H_2O_2 can be economically used through ultrasound-activatable catalase for burst-like O_2 release when required; catalase activity activated by ultrasound can reduce premature consumption of H_2O_2 and induce a more adequate H_2O_2 supply during SDT, which in turn more efficiently potentiates O_2 release and ROS generation. Different from previous approaches, such "lock and key" strategy could avoid many H_2O_2 molecules to be unavailable for O_2 enhanced SDT because of cell respiration. Although several drugs, such as glucose oxidase [28], engineered bacteria [29], β-lapachone [30], and nanoselenium [31], have been explored for the synthesis of H_2O_2 *via* different mechanisms, their generation procedure requires a high level of O_2 as a raw material, which is not well suited to SDT. For example, Dai *et al.* used a functional Dox@Pt prodrug Fe nanoparticles with nicotinamide adenine dinucleotide phosphate (NADPH) oxidases (NOXs) and superoxide dismutase (SOD) activity, which can colonize tumor regions and increase localized H_2O_2 generation by transferring electrons from NADPH to O_2.[32] In contrast to expanding the sources of H_2O_2, inhibiting unnecessary H_2O_2 expenditure may be a promising strategy to combat hypoxia before SDT treatment. Therefore, we propose a "H_2O_2-economizer" strategy for on-demand H_2O_2 decomposition-assisted O_2 generation instead of the currently prevalent O_2 supply approach. Such an H_2O_2 economizer is particularly important for enhancing SDT efficacy, which provides promising approaches to activate antitumor response [33].

Herein, we loaded the sonosensitizer chlorin e6 (Ce6) onto catalase-like Fe-PDAP (Fe-doped polydiaminopyridine), which was subsequently coated with the cancer cell membrane to design membrane-coated Fe-PDAP/Ce6 (MFC) for sonodynamic immunotherapy. As constructed, MFC was expected to possess the following favorable properties. 1) The Fe-PDAP in the MFC could simultaneously serve as the carrier and catalase-like nanozyme. 2) MFC could perform effective sonodynamic immunotherapy, which originated from an "H_2O_2 economizer"-mediated on-demand O_2 evolving process. The catalase-like activity of the MFC was significantly locked to reduce the unnecessary consumption of H_2O_2 in the TME. Upon irradiation with low-intensity focused ultrasound (US)[34, 35], whose acoustic beam is targeted and focused, the MFC can be selectively disassembled to liberate Fe-PDAP and recover the catalytic activity due to the cavitation effect. After that, the formed Fe-PDAP produces O_2 from intracellular H_2O_2, enabling efficient ROS production. The SDT process could release TAAs, which could promote dendritic cells (DCs) maturation to educate T cells. 3) MFC could target tumors with a high specificity using the cancer cell membrane due to its superiority in homologous targeting [22, 36, 37]. The cell membrane coating can keep the cargoes from eroding and reduce the preliminary leakage of camouflaged agents, which provides significant advantages in our study.[38, 39] Importantly, in combination with ICB therapy

(anti-programmed cell death protein-1 antibody, aPD-1), the MFC has demonstrated superb antitumor performance for both primary tumors and distant tumors (**Scheme 1**). Moreover, on-demand O_2-evolving sonodynamic immunotherapy with MFC induced minimal nonspecific damage to normal tissues, indicating high biocompatibility. Thus, this study provides an intriguing strategy that nanozymes can act as H_2O_2 economizers for on-demand O_2 evolution-assisted robust sonodynamic immunotherapy.

Methods and Materials

Reagents and Materials

Fe(III) chloride hexahydrate ($FeCl_3 \cdot 6H_2O$), $[Ru(dpp)_3]Cl_2$ (RDPP), and SOSG were purchased from Thermo Fisher Scientific (Los Angeles, CA, USA). Diamino pyridine (DAP) was obtained from Adamas-Beta (Shanghai, China). Amplex Red was provided by Aladdin Reagent Co., Ltd. (Shanghai, China). Ce6 was obtained from J&K Chemical Co. aPD-1 was provided by BioxCell (clone: RMP1-14, catalog no. BE0146). The membrane protein extraction kit, phenylmethanesulfonyl fluoride (PMSF), penicillin-streptomycin solution, trypsin, and DCFH-DA were purchased from Beyotime (Shanghai, China). DAPI was obtained from Boster Biological Technologies (Wuhan, China). A standard CCK-8 assay, calcein-AM, and PI were purchased from Dojindo (Japan). All materials were used as received without further purification.

Cell Lines

4T1 murine breast cancer cells, Panc-1 pancreatic cancer cells, HepG2 hepatocellular carcinoma cells and SKOV3 ovarian cancer cells were provided by Chongqing Medical University. 4T1 cells and SKOV3 cells were maintained in RPMI 1640 complete medium, and Panc-1 cells and HepG2 hepatocellular carcinoma cells were maintained in high-glucose DMEM supplemented with 10% FBS and 1% penicillin–streptomycin in a humidified atmosphere of 5% CO_2 at 37 °C.

Animals

Female BALB/c mice (6-8 weeks) were provided by the Animal Center of Chongqing Medical University. All animal studies were carried out under protocols approved by the Animal Ethics Committee of Chongqing Medical University.

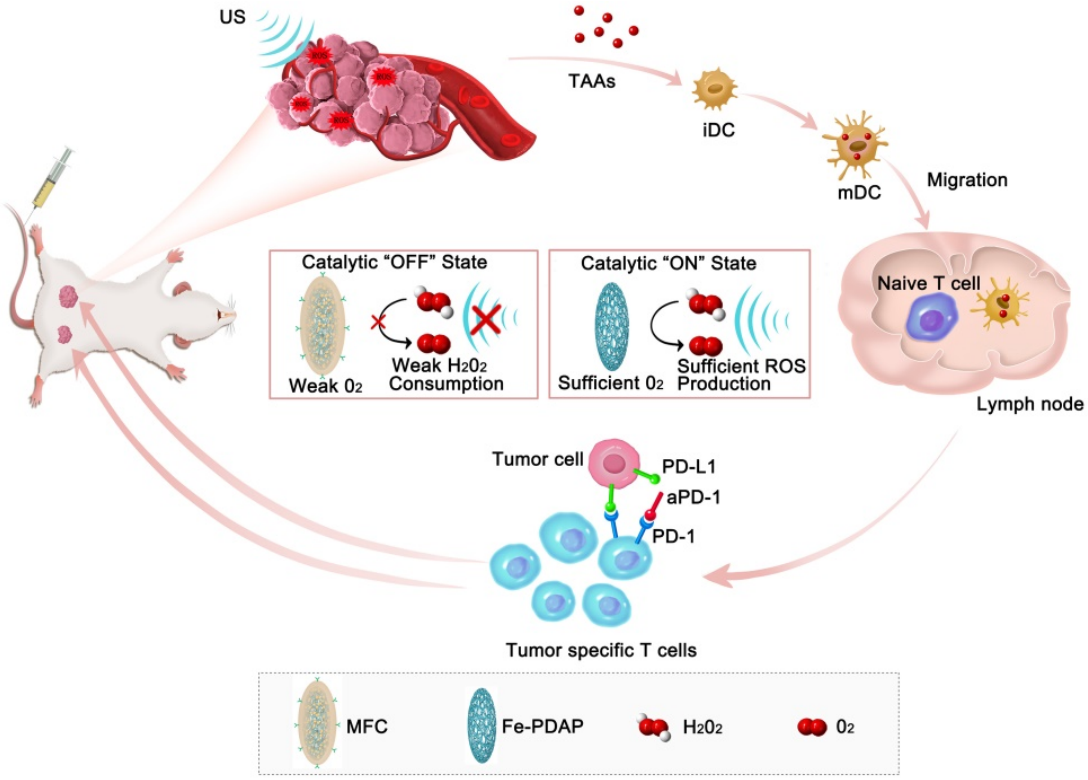

Scheme 1. Schematic illustration of the antitumor immune responses induced by MFC-based on-demand O_2-evolving SDT combined with immune checkpoint blockade for effective immunotherapy against cancer.

Extraction of Cancer Cell Membranes

Cell membranes were extracted using a membrane protein extraction kit according to the instructions provided by Beyotime Biotechnology. Briefly, cancer cells were seeded in cell culture dishes and scraped off with a cell scraper. The cells were collected by repeated centrifugation (1000 g, 5 min) and distributed into membrane protein extraction reagent pretreated with phenylmethanesulfonyl fluoride (PMSF) in an ice bath for 10-15 min. Afterward, the sample was subjected to repeated freeze-thawing, and centrifugated at 700g for 10min to collect supernatant. Finally, the supernatant was centrifuged (14000 g, 30 min) to obtain the cell membrane fragments.

Synthesis of Fe-PDAP

Fe-PDAP was synthesized through Fe(III)-mediated oxidative polymerization according to a previously reported method with modifications.[40] Briefly, $FeCl_3 \cdot 6H_2O$ (10 g) was dissolved in deionized water (200 mL) and sonicated for 10 min. DAP (1.0 g) was added to the mixture and stirred for 24 h at 37 °C to perform polymerization; the obtained mixture was purified with a dialysis bag (MW: 12 kDa) against distilled water overnight. Then, Fe-PDAP was obtained and stored at 4 °C for further use.

Synthesis of MFC

Ce6 was loaded onto Fe-PDAP by electrostatic adsorption and π-π interactions. In brief, Ce6 (40 mg) were dispersed in Fe-PDAP (60mg) dissolved in methyl alcohol, and magnetically stirred overnight at room temperature. Subsequently, the products were collected by centrifugation (12000 g, 10 min). After that, the obtained cancer cell membranes were mixed with as-prepared Fe-PDAP/Ce6 NPs, and an extrudation method was used to obtain MFC with the aid of a mini extruder (Avastin, Canada). The resulting MFC was further centrifuged to remove the remnants and stored at 4 °C for further use.

Characterization

TEM images were obtained with a JEM-1400plus (Japan). The particle size and zeta potential measurements were recorded on a Malvern Nano ZS90 (Malvern Instruments, UK). XRD images were taken on a PANalytical X'pert Power System (Spectris Pte. Ltd, Holland). XPS spectra were recorded on an ESCALAB 250 instrument (Thermo Fisher Scientific, USA). UV-Vis absorption spectra were acquired with a UV-Vis-NIR spectrophotometer (UV-3600, Shimadzu, Japan).

ROS Measurements *In vitro*

TEMP detected the ROS generated by MFC upon exposure to US irradiation. Typically, MFC (20 μg/mL Ce6) was exposed to US irradiation (1.0 MHz, 2 W cm^{-2}, 50% duty cycle) for 5 min in the presence of TEMP. The $^1O_2$ signal was immediately detected by the ESR spectrometer (JEOL-FA200). SOSG was introduced for the quantitative analysis of $^1O_2$ generation by MFC. Briefly, the SOSG solution was mixed with MFC solution (20 μg/ mL Ce6). Afterward, the mixture was irradiated by US (1.0 MHz, 2 W cm^{-2}, 50% duty cycle), and the fluorescence intensity of SOSG was detected with a multimode reader. Intracellular ROS levels were determined with DCFH-DA. DMTU was used to scavenge H_2O_2, and the concentration of DMTU was 20 μM. 4T1 cells were seeded into CLSM-exclusive culture dishes overnight and cocultured with different NPs for 4 h. Then, the cells were washed with PBS and incubated with DCFH-DA (2×10^{-5} M) for 30 min, followed by US irradiation (1.0 MHz, 2 W cm^{-2}, 50% duty cycle, 1 min). After another 20 min of incubation, the cells were observed by CLSM (λex/λem = 488 nm/530 nm).

In vitro Cytotoxicity Measurements

A standard CCK-8 assay was performed to characterize the cytotoxicity of MFC to 4T1 cells. Typically, the cells were cultured in 96-well plates (5×10^3 cells per well) overnight to adhere to the wells. Then, different concentrations of MFC were added and incubated for another 24 h, the CCK-8 assay was performed, and a multimode reader was used to determine the results. For the live/dead cell staining assay, 4T1 cells were seeded into CLSM-exclusive culture dishes (1×10^5 cells per dish) overnight and experienced different treatments. Then the cells were subjected to US irradiation (1.0 MHz, 2 W cm^{-2}, 50% duty cycle, 1 min). After that, the cells were stained with calcein-AM and PI for 15 min and observed by CLSM.

Cellular Uptake Performance of MFC

4T1 cells were seeded in CLSM-exclusive culture dishes overnight and then incubated with different MFCs (cancer cell membranes from different cells) for 1 h. Afterward, the cells were washed with PBS, fixed with 4% paraformaldehyde for 15 min, and incubated with DAPI before observation by CLSM. Excitations: 630 nm for Ce6 and 405 nm for DAPI; emissions: 670 nm for Ce6 and 455 nm for DAPI. Cellular uptake was further evaluated by ICP-MS (Agilent ICPMS 7700) based on the above protocols.

Determination of Catalytic O_2 Generation Ability

Different NPs were dispersed in an aqueous solution containing H_2O_2 without or with US irradiation (1.0 MHz, 2 W/cm^2, 50% cycle, 3min). The oxygen concentration was monitored with a dissolved oxygen meter (Mettler Toledo, China). The intracellular production of O_2 was characterized by an RDPP probe, whose luminescence can be quenched by oxygen. Briefly, 4T1 cells were seeded into CLSM-exclusive culture dishes (1×10^5 cells per dish) and cultured overnight. The cells were then incubated with RDPP (10 μM) for 4 h, incubated with NPs, and treated with or without US (1.0 MHz, 2 W/cm^2, 50% cycle, 3min). Finally, fluorescence images were captured by CLSM under excitation at 488 nm.

Evaluation of H_2O_2 Consumption Ability

Different NPs (200 μg/mL) were dispersed in an aqueous solution containing H_2O_2 without or with US irradiation (1 MHz, 2 W cm^{-2}, 50% cycle, 3min). Amplex Red (200 μM) and HRP (0.2 U/ L) were added, and the absorbance of the mixture solution at 590 nm was monitored. 4T1 cells were seeded in a 12-well plate and cultured overnight to evaluate intracellular H_2O_2. Then, the cells were coincubated with various NPs for 3 h and exposed to US irradiation (1 MHz, 2 W cm^{-2}, 50% cycle, 3min). The cells were collected and broken up with an ultrasonic probe (Sonics & Materials, Inc., USA). Finally, Amplex Red (200 μM) and HRP (0.2 U/ L) were added, and the absorbance at 590 nm was detected.

Detection of Tumor Hypoxia Status *In vivo*

Intratumoral blood oxygen saturation was evaluated with a Vevo LAZR PAI system (Visual Sonics Inc., Toronto, Canada). Oxygen saturation inside the tumors was measured at the indicated time points after intravenous injection of NPs using Oxyhem mode with excitation wavelengths of 750 and 850 nm. The expression level of HIF-1α was measured by immunofluorescence staining and western blotting at the indicated time points.

Biodistribution Study of MFC *In vivo*

4T1 tumor-bearing mice were intravenously injected with MFC (3 mg/mL), and fluorescence images were acquired at the indicated time points (1, 2, 4, 6, 8, and 24 h) using a fluorescence live imaging (FLI) system (Xenogen IVIS Spectrum, PerkinElmer, USA). The tumors and major organs (including the heart, liver, spleens, kidneys, and lungs) were imaged *ex vivo* 24 h post-injection.

In vivo Anticancer Therapy

4T1 cell suspensions (1×10^6) were inoculated into the right mammary fat pad of each mouse as the primary tumor to establish an orthotopic breast cancer model. Four days later, 4T1 cell suspensions (5×10^5) were inoculated into the left mammary fat pads of mice as distant tumors. When the first tumor reached 50-100 mm^3 in volume, the mice were randomly distributed into 6 groups and intravenously administered NPs at a dose of 4 mg/mL on days 0, 3, and 6. DMTU was used to scavenge H_2O_2, and the concentration of DMTU was 20 μM. For groups treated with US irradiation, US (1.0 MHz, 2W cm^{-2}, 50% duty cycle, 3 min) irradiation was applied to the mice 4 h and 24 h after injection. aPD-1 antibodies at a dose of 100 μg per mouse were intraperitoneally injected on days 1, 4, and 7. Tumor sections of the primary and distant tumors were harvested for H&E and TUNEL staining. The tumor sizes were measured with a Vernier caliper every other day, and the volume was calculated as (width^2 × length)/2. The body weights of the mice were measured every other day. On day 16, one mouse in each group was sacrificed, and the major organs were collected for H&E staining.

Ex vivo Analysis of Different Groups of Immune Cells

The mice were sacrificed, and then tumor-draining lymph nodes and the distant tumors were harvested on day 8 to explore the underlying immune mechanism of therapy. The tumor-draining lymph nodes were quickly cut into fragments and stained with APC-CD11c (Biolegend, catalog: 117310), FITC-CD80 (Biolegend, catalog: 104705), and PE-CD86 (Biolegend, catalog: 105007). The tumor tissues were quickly cut into fragments, digested with a mixture containing 2% fetal bovine serum (Pan, Germany), 0.02% collagenase IV, and 0.002% DNase I (Solarbio, Beijing, China), ground using the rubber end of a syringe and filtered through a 40 μm nylon cell strainer (NEST, Wuxi, China) to prepare the single-cell suspension. Following removal of the red cells *via* red blood cell lysis buffer and rinsing with PBS, the single-cell suspension was stained with a fluorescently labeled antibody according to the manufacturer's protocols. To analyze CD8$^+$ T cells, the cells were labeled with live-dead BV421 (Biolegend, catalog: 423114), CD45-APC-Cy7 (Biolegend, catalog: 103116), CD3-FITC (Biolegend, catalog: 100204), CD4-Percp (Biolegend, catalog: 100431), and CD8-APC (Biolegend, catalog: 100711). The cells were labeled with CD4-FITC (eBioscience, catalog: 11-0041-82), CD25-PE-Cy7 (eBioscience, catalog: 25-0251-82), and Foxp3-PE (eBioscience, catalog:

12-4771-82) to analyze Tregs ($CD4^+CD25^+Foxp3^+$). After different treatments, the mice were sacrificed, and the distant tumors were collected, homogenized, and centrifuged to harvest the supernatant on day 8. Cytokines were analyzed with ELISA kits according to the vendor's instructions (Dakewe Biotech, China).

In vivo Biosafety of MFC

Healthy female Kunming mice (6-8 w) were intravenously administered MFC at a dose of 4 mg /mL. Untreated healthy Kunming mice served as controls (n = 4). The mice were then sacrificed at 1 day, 7 days, 14 days, and 21 days after injection. Blood samples were taken, and the major organs (heart, liver, lung, spleen, and kidney) were harvested for multiple evaluations, including routine blood tests, serum biochemistry analysis, and H&E staining.

Statistical Analysis

All data are presented as the mean ± standard deviation (SD), and statistical analysis of the data was performed by Student's t-test and one-way ANOVA. $^*p < 0.05$, $^{**}p < 0.01$, $^{***}p < 0.001$.

Results and Discussion

Synthesis and Characterization of MFC

Fe-PDAP with catalase-like activity was prepared using a Fe(III) mediated oxidative polymerization strategy (**Figure 1A**). Transmission electron microscopy (TEM) images and scanning electron microscopy (SEM) images revealed fusiform-like shaped Fe-PDAP with a uniform morphology (**Figure 1B-D**). The obtained Fe-PDAP (polydispersity index, PDI:0.234) showed a narrow hydrodynamic size distribution of approximately 40 nm and a positive charge potential of +39 mV (**Figure 1H-I**). Then, we placed the Fe-PDAP aqueous solution in a dialysis bag, and the solution was replaced with methanol at room temperature for subsequent loading of Ce6. Ce6 was loaded onto Fe-PDAP through hydrophobic and π-π interactions after stirring in a methanolic solution to prepare Fe-PDAP/Ce6 (FC). After loading, the size distribution of FC (PDI:0.215) increased to approximately 60 nm (**Figure 1H**), and its zeta potential reversed to +4.59 mV (**Figure 1I**), which indicates the successful loading of Ce6. However, the loading agents can hardly be observed under TEM, most likely because the layer has a low electron density (**Figure S1**). The cracked cell membranes extracted from the 4T1 cells were used as the shells of FC to prepare cancer cell membrane-coated FC (MFC, PDI:0.18) through a facile coextrusion method. Compared to naked FC, MFC showed a prominent core-shell structure with a uniform lipid bilayer on the shell, indicating the successful cloaking of the cancer membrane (**Figure 1E-G**). Moreover, coating cancer cell membranes to FC led to a mild increase in hydrodynamic size and a positive-to-negative reversal of zeta potential (**Figure 1H-I**). In addition, compared to that of free Ce6, the UV-Vis absorption spectra of MFC showed a slight red-shift phenomenon from 660 to 665 nm, which revealed electrostatic adsorption and π-π interactions between Ce6 and Fe-PDAP (**Figure 1J**). According to the UV-Vis analysis, we calculated the encapsulation efficiency of Ce6 as 72%, and the loading capacity of Ce6 was 48%. (**Figure S2**). The color discrepancy between Fe-PDAP and MFC further confirmed the successful loading of Ce6 (**Figure S3**). We have also examined the stability of MFC in different mediums. The results showed that the size of MFC remained unchanged in H_2O and 1640 containing 10% FBS wihtin 15 days (**Figure S4**), indicating the high stability of MFC. No noticeable difference was found between the powder X-ray diffraction (XRD) patterns of Fe-PDAP and MFC, suggesting a negligible effect of the loading process on the crystal structure of Fe-PDAP (**Figure 1K**). The peak of Fe-PDAP was recognized with akaganeite according to the standard XRD card. The typical binding energy peaks of $Fe^{1/2}$ and $Fe^{3/2}$ in the X-ray photoelectron spectroscopy (XPS) showed that approximately 100% Fe in MFC was in the chemical state of Fe(III) (**Figure 1L, Figure S5**). Fe(III) could reduce the toxic Fenton reaction and improve the biosafety of the MFC after exposure to an acidic environment. Elemental mapping analysis confirmed the existence of Fe in the MFC (**Figure 1M**), and we obtained an Fe content of 3.93 wt% according to inductively coupled plasma mass spectrometry (ICP-MS) results.

In vitro On-demand Catalase Activity of the NPs and the H_2O_2 content during treatment

Under US irradiation, MFC showed an evident US-responsive burst of Ce6 release, with a total Ce6 leakage of approximately 80% after repeated US irradiation, which could be ascribed to US-induced MFC disintegration (**Figure 2A**). In comparison, the Ce6 release rate was relatively low (~20%) without US treatment, indicating the excellent chemical stability of MFC. The morphology of US-treated MFC was also tested, and the core-shell structure was broken under TEM observation (**Figure 2B**), which could be ascribed to acoustic radiation forces and cavitation effect induced disintegration.[41, 42] US-treated MFC showed a decrease in hydrodynamic size and a negative-to-positive reversal of zeta potential, also confirming the breakage of the core-shell structure (**Figure S6**). As such, both the the removal of cell membrane or the detachment of Ce6 was achieved

and the exposure of Fe-PDAP can initiate catalytic effect.

Since H_2O_2 content has a powerful influence on O_2 generation during SDT treatment, it is essential to confirm the catalytic activity changes upon US irradiation under MFC treatment (**Figure 2C**). We evaluated the catalase activity of Fe-PDAP with a portable dissolved oxygen meter after the addition of H_2O_2. As expected, a noticeable increase in the concentration of dissolved O_2 suggested that Fe-PDAP could decompose H_2O_2 (**Figure S7**). However, the decoration process substantially blocked the catalytic effect of Fe-PDAP, and minimal O_2 generation was detected, indicating that the decoration process reduced the consumption of H_2O_2 (**Figure 2D**). The US-detachable properties of MFC inspired us to test the influence of US on the catalytic effect. It was fascinating to find that US treatment could significantly enhance the catalytic effect of MFC, and recover to reach the ability of naked Fe-PDAP (**Figure S8**). Next, we employed Amplex Red to test the H_2O_2 content both extracellularly and intracellularly under different treatments.[43, 44] After the H_2O_2 solution was treated with Fe-PDAP, noticeable H_2O_2 depletion was observed compared to the control groups (MFC or FC alone), confirming that the H_2O_2 depletion capability was reduced by the decoration process (**Figure 2E**). In addition, in the group treated with MFC+US, the H_2O_2 content was comparable to that of the Fe-PDAP alone group. These results revealed that MFC could reduce H_2O_2 consumption, and US could achieve on-demand catalysis to enhance the O_2 supply during SDT. Similarly, we evaluated intracellular H_2O_2

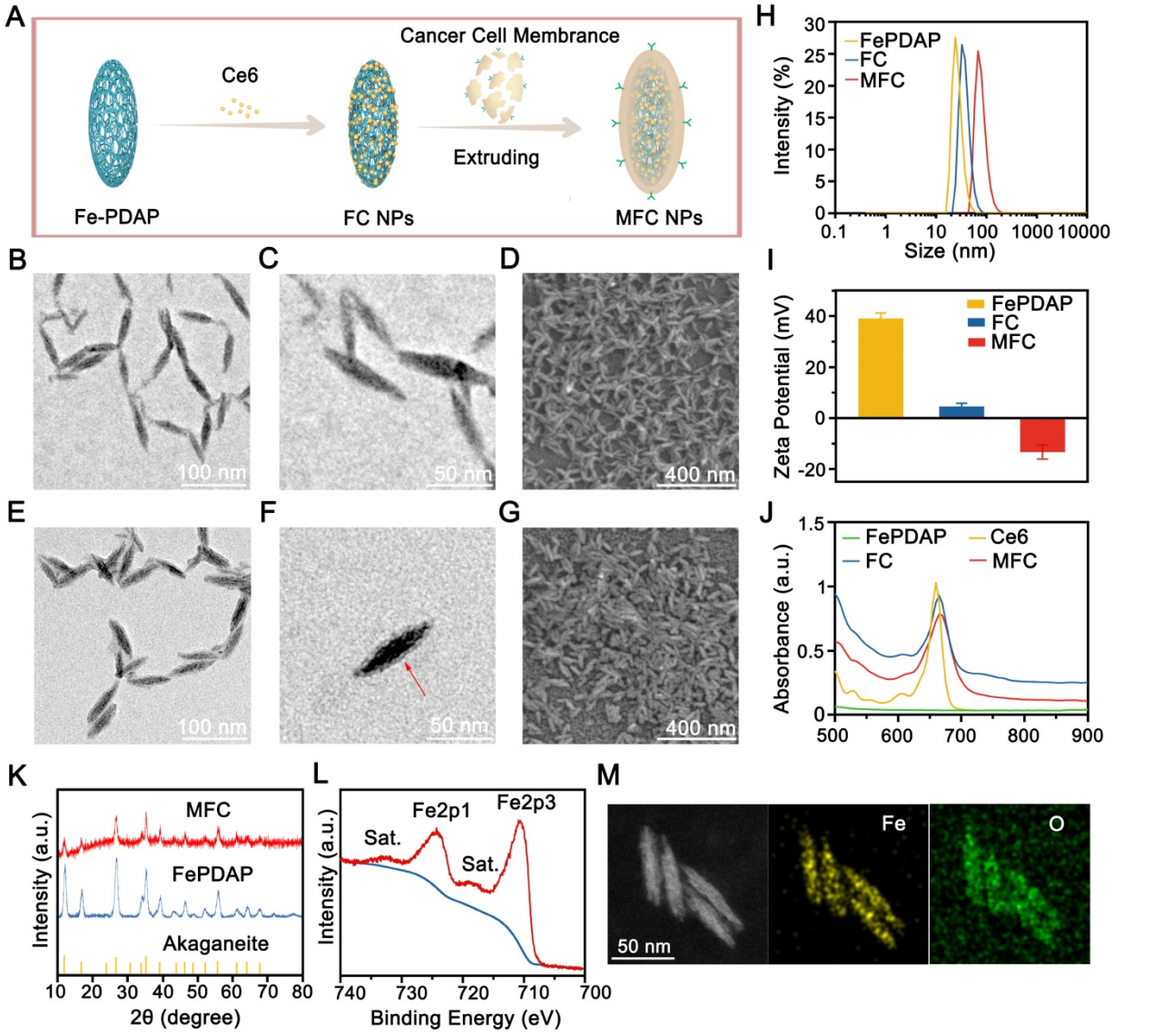

Figure 1. MFC characterization. (A) Schematic illustration of the synthetic procedures for engineered MFCs. (B-D) TEM and SEM images of Fe-PDAP. (E-G) TEM and SEM images of MFC. (H) Size distribution of Fe-PDAP, FC, and MFC. (I) Zeta potentials of Fe-PDAP, FC, and MFC. (J) UV/vis absorption spectra of Fe-PDAP, Ce6, FC, and MFC. (K) XRD patterns of MFC and Fe-PDAP. (L) XPS high-resolution Fe2p spectrum of MFC. (M) Elemental mappings of MFC.

consumption under different treatments. There was reduced H_2O_2 consumption in the MFC group, and the groups treated with MFC+US showed H_2O_2 consumption similar to that of the Fe-PDAP group (**Figure 2F**). These phenomena enable on-demand depletion of H_2O_2 and provide an excellent method for supplying O_2 to overcome tumor hypoxia. The effectiveness of MFC+US in achieving on-demand O_2 production was further investigated in 4T1 cells using an RDPP probe, whose fluorescence can be quenched by intracellular O_2.[45] The results showed that the 4T1 cells incubated with naked Fe-PDAP or MFC+US showed notably quenched fluorescence compared with the other groups. The drastic H_2O_2 decrease in the MFC+US group supports our hypothesis that US-treated MFC could improve hypoxia relief in tumor cells by on-demand oxygen supply (**Figure 2G, Figure S9**).

To explore the limited time for the release of Fe-PDAP, MFC and the main composition of MFC (including Fe-PDAP, Ce6, and cancer cell membrane) were co-incubated with 4T1 cells, and different ultrasonic irradiation time was performed. The MFC treated groups were set as the on-demand O_2 supply group, while the solution treated with Fe-PDAP, Ce6, and cancer cell membrane was set as the currently prevalent O_2 supply approach group. To confirm the content of Ce6 was equivalent in the two groups, CLSM was carried out to observe the fluorescence intensity. A 2 times amount of Ce6 in the currently prevalent O_2 supply approach group (including Fe-PDAP, Ce6, and cancer cell membrane) was added to achieve the same fluorescence intensity between the two groups. After 4 h of incubation, a higher level of ROS generation in the MFC groups was observed in all the observation times from the 30s to 90s (**Figure S10**), indicating a higher ROS generation capability of MFC with the assistance of ultrasound. Therefore, we believe the on-demand oxygen supply method for enhancing sonodynamic therapy is highly efficient.

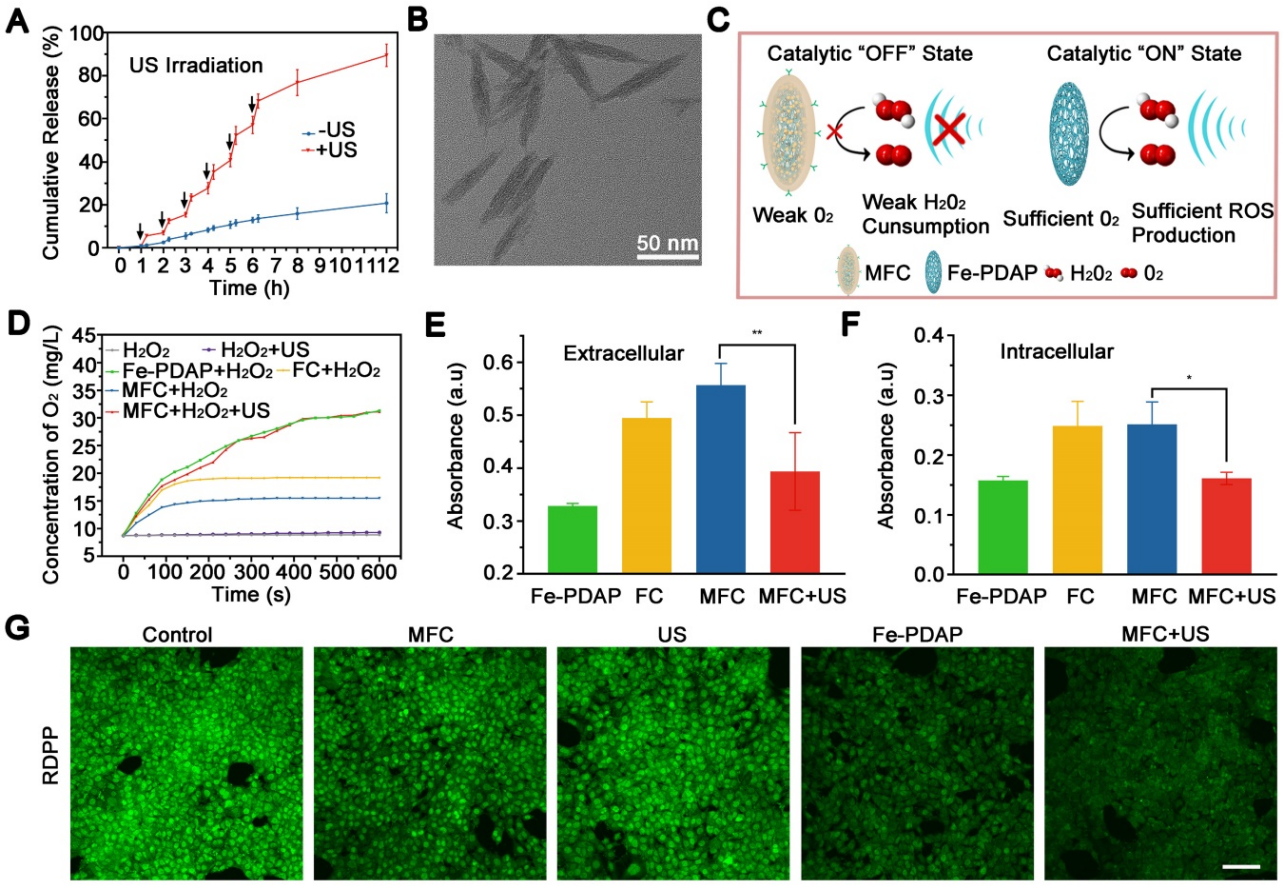

Figure 2. *In vitro* on demand catalase-like activity of the NPs and the H_2O_2 content during treatment. (A) Ce6 controlled release of MFC triggered by US irradiation. (B) TEM of MFC after US exposure. (C) Schematic illustration of the therapeutic mechanism in the presence of US-detachable catalase-like nanozymes. (D) The production of O_2 by different NPs with or without US irradiation. (E) Extracellular H_2O_2 content after different treatments measured by Amplex Red. (F) Intracellular H_2O_2 content after different treatments measured by Amplex Red. (G) Confocal laser scanning microscopy (CLSM) images of RDPP in 4T1 cells after different treatments. Scale bar: 100 μm.

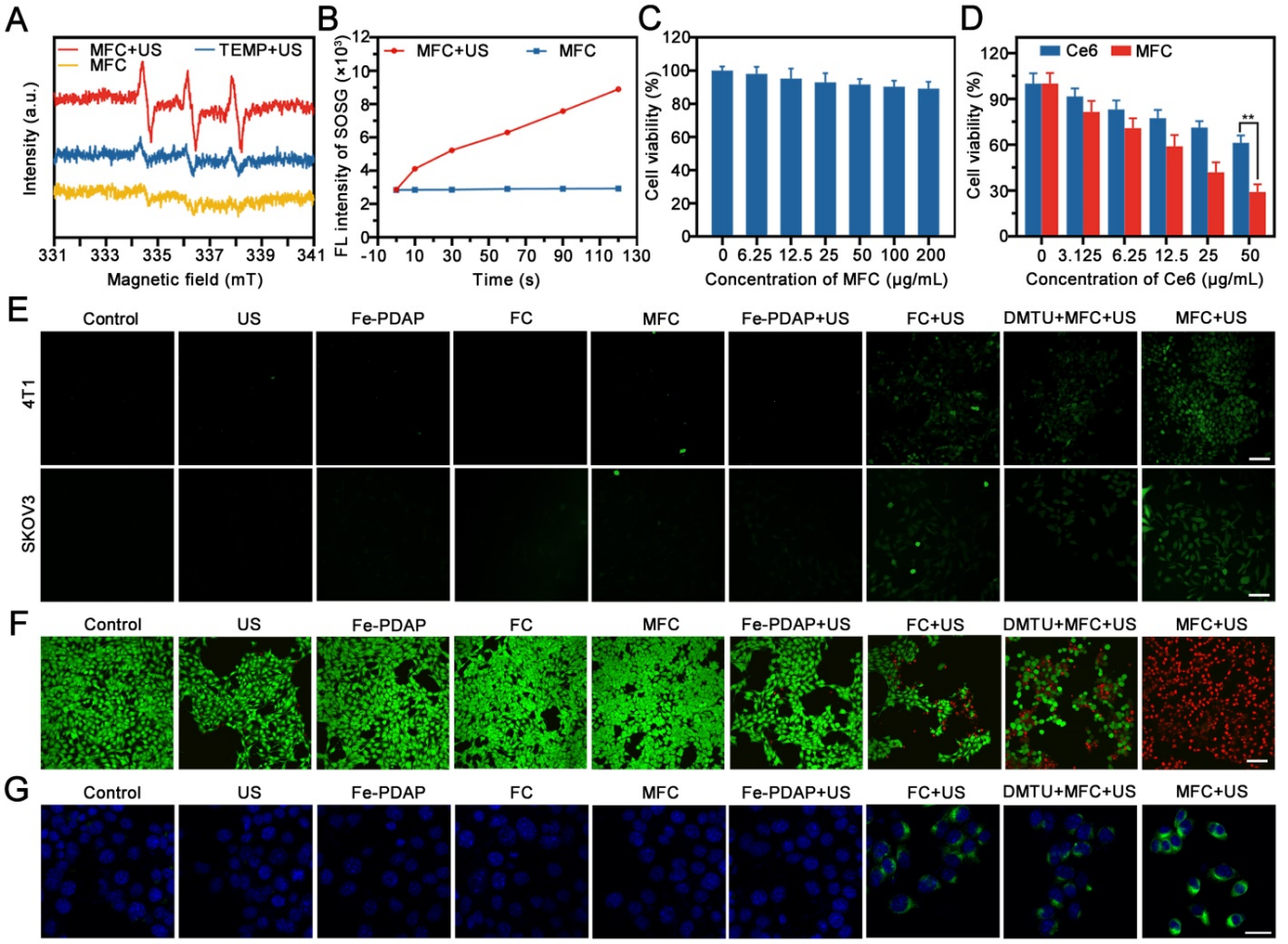

Figure 3. *In vitro* cytotoxicity assay and therapeutic effects. (A) ESR spectra of MFC with or without US irradiation. (B) Quantitative analysis of ROS production by MFC with or without US irradiation using SOSG as a probe. (C) Cell viability of 4T1 cells after incubation with MFC for 24 h. (D) Cell viability of 4T1 cells after treatment with Ce6 or MFC at various concentrations of Ce6 after exposure to US irradiation. (E) CLSM images of 4T1 cells and SKOV3 cells stained with DCFH-DA after different treatments among different groups. Scale bar: 100 μm. (F) CLSM images of 4T1 cells costained with PI and calcein-AM after different treatments. Scale bar: 100 μm. (G) Representative CLSM images showing CRT exposure on 4T1 tumor cells after different treatments. scale bar = 25 μm.

In vitro Cytotoxicity Effects of On-Demand Sonodynamic Therapy.

We first evaluated the therapeutic activity of MFC *in vitro* by testing US irradiation-induced ROS generation with electron spin resonance (ESR) spectroscopy. The results showed that the US could efficiently excite MFC to generate ROS (**Figure 3A**). Moreover, the singlet oxygen sensor green (SOSG), which possesses high specificity for $^1O_2$, was used as a ROS probe to detect the generation of $^1O_2$ under US irradiation. All tested time points showed fluorescence enhancement after US irradiation and a time-dependent signal intensity enhancement (**Figure 3B**). Next, we studied the *in vitro* biosafety of MFC using a standard cell counting kit-8 (CCK-8) assay. Negligible cytotoxicity was observed toward 4T1 cells after incubation for 24 h (**Figure 3C**). In addition, the hemolysis assay results showed that the MFC has high biosafety for *in vivo* applications (**Figure S11**). The *in vitro* cytotoxicity of MFC or Ce6 irradiated by US activation was also evaluated by CCK8 assay. The cell viability of all treatment groups decreased with increasing Ce6 concentration, indicating that the therapeutic effect was concentration-dependent (**Figure 3D**). The harmful ROS in tumor cells is considered the most representative therapeutic unit to induce intracellular oxidative stress and cell death. Therefore, the intracellular ROS levels after incubation with MFC were detected using 2′,7′-dichlorofluorescein diacetate (DCFH-DA), a ROS indicator that can be converted to 2′,7′-dichlorofluorescein (DCF) and emits green fluorescence under CLSM observation. 1, 3-Dimethylthiourea (DMTU) was used to scavenge H_2O_2 and mimic a microenvironment lacking H_2O_2. [46]There was a significant fluorescence signal in the MFC+US group (**Figure 3E, Figure S12**). In contrast, much weaker fluorescence was observed in the DMTU+MFC+US group, indicating that MFC could initiate more effective ROS generation and H_2O_2 plays an essential role in enhancing SDT. Additionally, to intuitively

observe the distribution of live and dead 4T1 cells, the fluorescent dyes calcein-AM (green) and propidium iodide (PI) (red) were used.[47] The results showed that 4T1 cells could be killed more efficiently in the MFC+US group than the other groups after 4 h of incubation, demonstrating the effectiveness of MFC in on-demand producing intracellular ROS for tumor therapy (**Figure 3F, Figure S13**). To make the evaluation of on-demand sonodynamic therapeutic efficacy more persuasive, we have built another tumor cells (SKOV3 cells) for further evaluation. The therapeutic efficacy in SKOV3 cells was highly consistent with the results presented in 4T1 cells. Therefore, we believe that our on-demand sonodynamic therapy has the potential to be extended to other tumors. Immunogenic cell death (ICD) has been regarded as a requirement for effective immunotherapy. Calreticulin (CRT) is a significant biomarker of ICD. It has been reported that the intracellular oxidative stress caused by SDT could potentially trigger CRT expression on the surface of tumor cells, increase the immunogenicity of tumors and mobilize the immune system. Therefore, the expression of cell surface CRT induced by MFC-enhanced SDT was evaluated by CLSM *in vitro*. The MFC+US group showed the highest CRT expression on the surface of tumor cells, which could be ascribed to massive intracellular ROS generation (**Figure 3G**). The results indicated that MFC-enhanced SDT could efficiently induce ICD and activate the immune system.

Tumor Hypoxia Status Detection *In vivo*

The *in vivo* catalytic behavior of MFC was systematically evaluated using photoacoustic imaging (PAI). This noninvasive method can discriminate oxygenated hemoglobin from deoxygenated hemoglobin according to the absorbance spectrum.[48] As shown in **Figure 4A**, minimal oxyhemoglobin signal intensities were observed in the control and US-only groups, indicating that the US alone could not induce O_2 generation in the tumor microenvironment. In contrast, the Fe-PDAP group showed enhanced oxyhemoglobin signal intensities within the tumor region, confirming that the presence of Fe-PDAP could improve oxygenation in hypoxic tumors *via* the decomposition of excess H_2O_2. Notably, the oxyhemoglobin signal intensities of the MFC group were significantly lower than those of the Fe-PDAP alone group, indicating that the catalytic activity was remarkably inhibited by the surface-modified structure (**Figure 4B-C**). However, US treatment led to significantly increased MFC catalytic activity, producing the highest blood oxygen saturation among the groups. The above results suggested that decoration on the Fe-PDAP surface could avoid additional H_2O_2 consumption and that US irradiation could switch on the enzymatic activity of Fe-PDAP to afford robust SDT through on-demand O_2 supply.

To further verify the relief of tumor hypoxia induced by MFC+US, tumors were collected 24 h after various treatments for immunofluorescence staining of HIF-1α. As shown in **Figures 4D** and **4E**, the HIF-1α signals showed a reduction in the tumors injected with Fe-PDAP. Comparatively, the tumor tissue treated with MFC+US showed a more weakened expression of HIF-1α during the observation period. These results indicated that decoration of Fe-PDAP could achieve on-demand oxygen production with US assistance and indeed lead to robust tumor hypoxia relief. Furthermore, the expression of HIF-1α was also investigated by western blot analysis. The results showed that the expression of HIF-1α/β-actin was significantly reduced in the MFC+US group compared to the MFC-only group and the control group (**Figure S14**), indicating that US-treated MFC provides significant hypoxia alleviation for O_2-assisted SDT. Moreover, the expression of HIF-1α/β-actin in the MFC-only group was almost the same as that in the control group, suggesting that the catalytic activity of MFC was almost turned off. Therefore, the remarkable SDT effect and on-demand tumor oxygenation enhancement observed with MFC could ensure potent tumor inhibition.

Homologous Targeting Properties of MFC

Functionalized adhesion proteins on the cancer cell membrane have been considered critical for achieving specific homologous targeting ability. To investigate the homotypic targeting effects of the cancer cell membrane, we first evaluated the overall protein components of MFC by sodium dodecyl sulfate-polyacrylamide gel electrophoresis (SDS-PAGE). The results showed that MFC retained almost all the proteins from the original 4T1 cell membrane, indicating minimal protein loss during the decoration process (**Figure 5A**). To assess the homologous targeting effects of the MFC, the cellular uptake of FC and MFC was conducted on 4T1 cells and observed by CLSM. The MFC group showed stronger Ce6 fluorescence in the cytoplasm of 4T1 cells than that of FC group (**Figure 5B-C**). To further evaluate the homologous targeting effects of the MFC, the prepared FC was decorated with different cell membranes, and CLSM and ICP-MS were used to assess internalization by 4T1 cells. FC cloaked with PANC-1 pancreatic cancer cell membranes (PANC-1M), HepG2 hepatocellular carcinoma cell membranes (HepG2M), or 4T1 breast cancer cell

membranes (4T1M) were incubated with 4T1 cells for 1 h. The results showed obvious Ce6 fluorescence in the 4T1M group in the cytoplasm of 4T1 cells, whereas much weaker fluorescence was found in both the PANC-1M and HepG2M groups (**Figure 5D-E**). The marked differences in red fluorescence among these treatments demonstrated that the 4T1 cancer cell membranes exhibited the highest affinity for homologous cells because the as-prepared MFC displayed the same cell adhesion molecules as the original cancer cells. The superior homologous targeting properties of MFC were also confirmed by ICP-MS, in which the cells treated with the 4T1M-originated MFC had an average Fe content of 1.6 mg/mL, which was almost 3 times higher than that of the PANC-1M- or HepG2M-originated MFCs (**Figure 5F**).

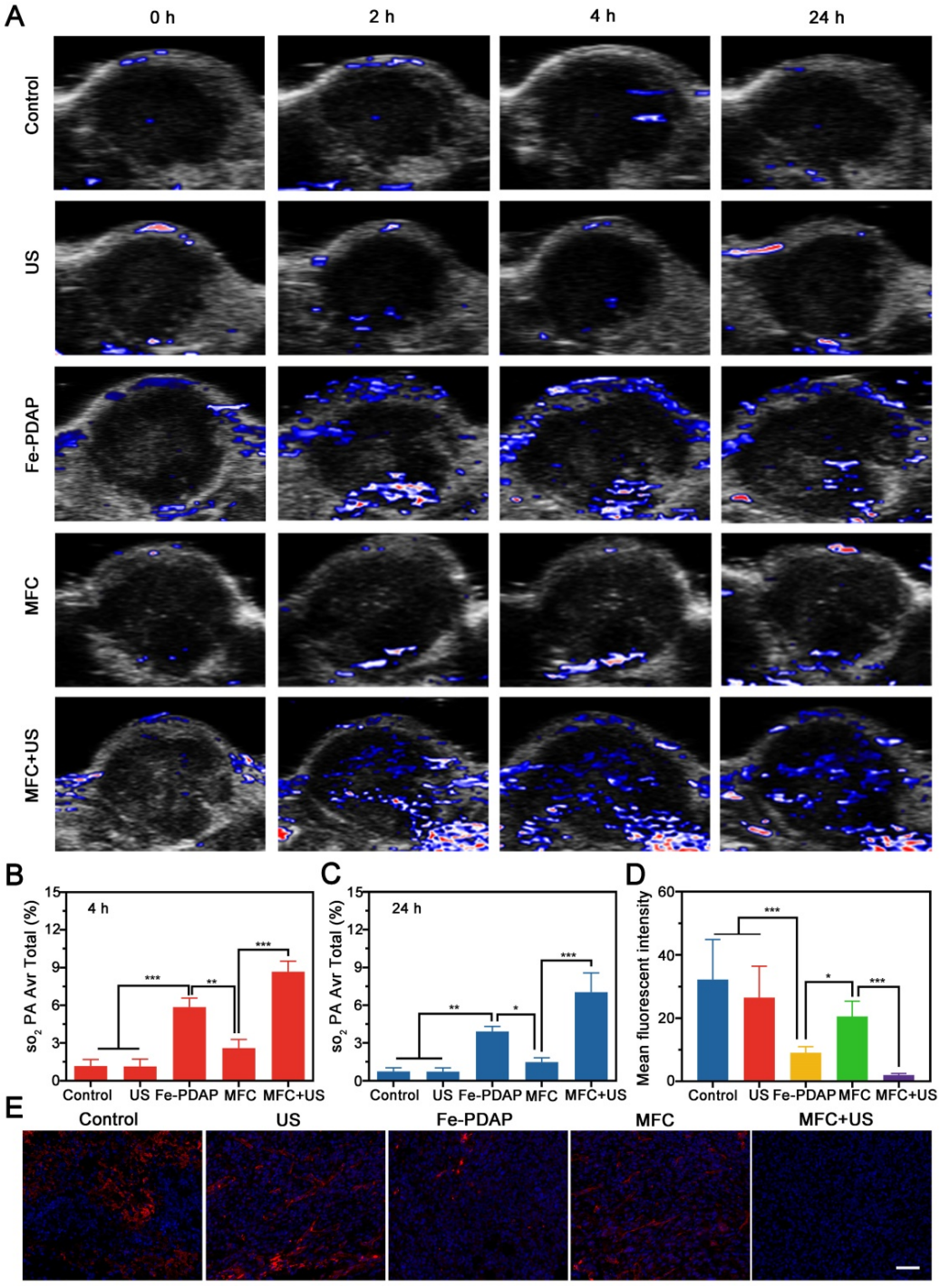

Figure 4. *In vivo* hypoxia relief after different treatments. (A) Representative PA images of tumor sites in 4T1 tumor-bearing mice after various treatments and the corresponding signal intensity values at (B) 4 h and (C) 24 h. (D-E) Representative immunofluorescence images of tumor sections stained with a HIF-1α after different treatments and the corresponding signal intensity values. Scale bar: 50 μm.

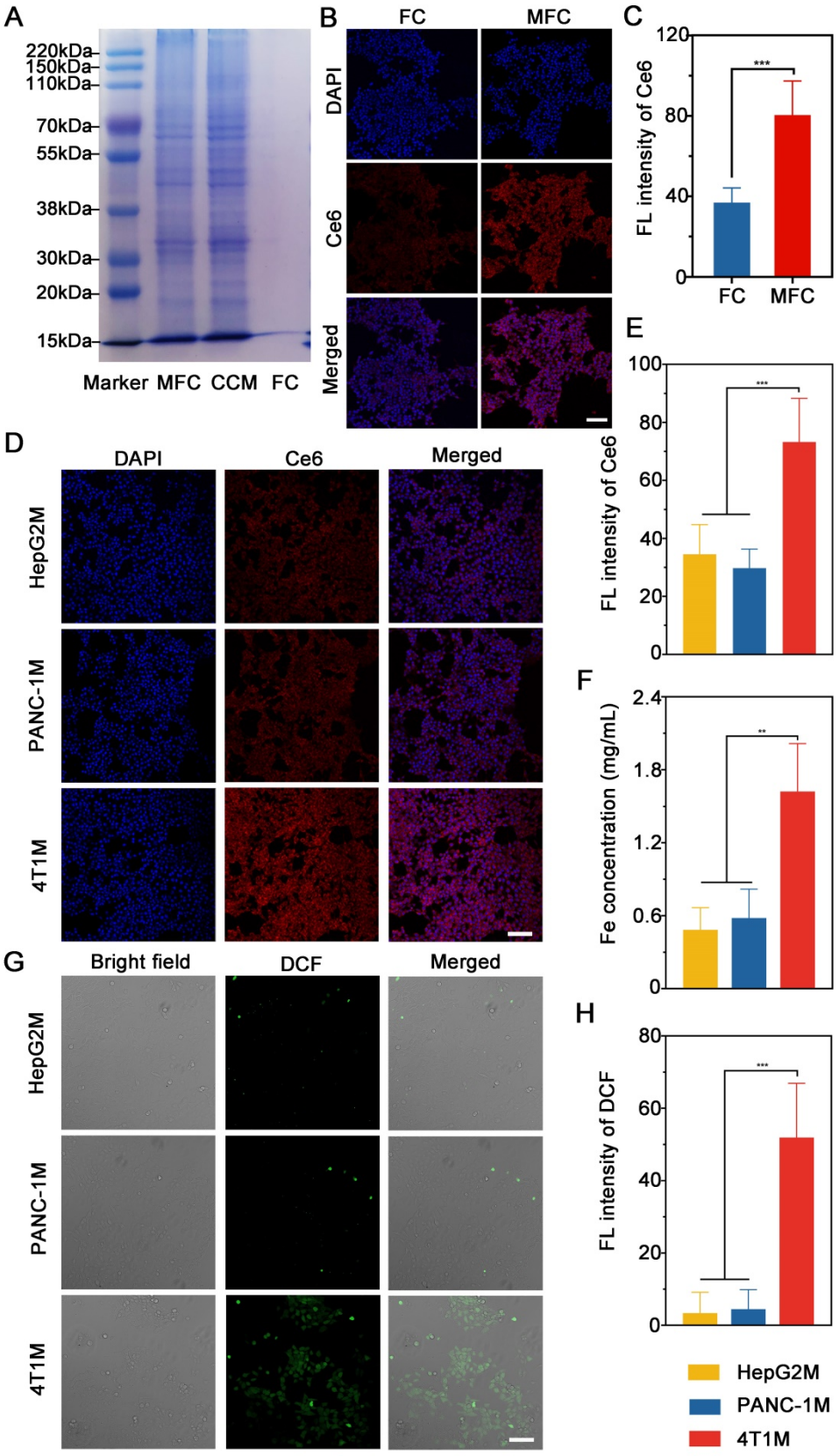

Figure 5. *In vitro* active targeting effects of MFC. (A) SDS-PAGE analysis of MFC, cancer cell membranes, and FC. (B-C) CLSM images of the 4T1 cells incubated with FC and MFC, and the corresponding quantitative fluorescence intensity of Ce6. Scale bar: 100 μm. (D-E) CLSM images of 4T1 cells treated with FC cloaked with different cancer cell membranes and the corresponding quantitative fluorescence intensity of Ce6. Scale bar: 100 μm. (F) Intracellular Fe content in 4T1 cells after treatment with FC cloaked with different cancer cell membranes. (G-H) CLSM images of 4T1 cells stained with DCFH-DA after treatment with FC cloaked with different cancer cell membranes and the corresponding fluorescence intensity of DCF. Scale bar: 100 μm.

After validating the homologous targeting properties of MFC NPs on 4T1 cells, we further studied their functional role in antitumor SDT separately using heterologous membranes as controls. Contrary to decoration with PANC-1M or HepG2M, 4T1M decoration showed significantly enhanced DCF fluorescence with US irradiation under the same conditions. These findings further validated the effectiveness of tumor-specific therapy *in vitro* for further sonodynamic immunotherapy (**Figure 5G-H**). Thus, the results above supported our conclusion that the MFC originating from 4T1M could effectively be enriched in 4T1 cells *via* homologous targeting mechanisms, further demonstrating the particularly strong binding and/or uptake efficiency of NPs by their original cells.

In vivo Evaluation of On-demand Oxygen Production-Assisted Sonodynamic Immunotherapy

FL imaging was used to evaluate tumor accumulation and biodistribution of MFC. MFC was intravenously injected into mice bearing orthotopic 4T1 tumors and observed by an *in vivo* imaging system. The fluorescence signal in the tumor was detected 1 h after injection of MFC, and a high accumulation of MFC in the tumor was recorded, reaching a peak at 4 h post-injection and gradually decreasing after 4 h of observation, demonstrating an optimized time window for SDT (**Figure S15**). Even up to 24 h after injection, the tumor tissues retained high uptake of MFC, as evidenced by the fluorescence signal (**Figure S16**). Therefore, the tumor-bearing mice were subjected to US irradiation at 4 h and 24 h after intravenous injection of the MFC.

Next, we investigated the potential of MFC for sonodynamic immunotherapy with a 4T1 tumor model, as shown in a schematic illustration (**Figure 6A**). Briefly, a murine orthotopic tumor model was established by injecting 4T1 cells into the right mammary fat pad of female BALB/c mice (the primary tumor). After 4 days of incubation, a second tumor was injected into the left side of the mammary fat pad (as the distant tumor). The mice with 4T1 orthotopic tumors were divided into six groups and treated with PBS, MFC, aPD-1, MFC+US, DMTU+MFC+US+aPD-1, or MFC+US+aPD-1. aPD-1 at a dose of 100 μg/mouse was injected intraperitoneally on the 1st, 4th, and 7th days. The lack of H_2O_2 content in the tumor microenvironment is often accompanied by resistance to sonodynamic therapy due to their ability to produce O_2. Therefore, DMTU was intratumorally injected into the primary tumor 24 h before treatment to scavenge H_2O_2 and mimic a tumor microenvironment lacking H_2O_2. We found that MFC+US could inhibit the growth of the primary tumors (**Figure 6B, Figure S17**). However, sonodynamic therapy alone failed to inhibit the distant tumors (**Figure 6C, Figure S17**). After combination with aPD-1, MFC-reinforced SDT+aPD-1 more effectively suppressed both primary and distant tumors (**Figure 6D-6E**), further demonstrating the excellent tumor inhibition efficacy of sonodynamic immunotherapy. Comparatively, DMTU+MFC+US+aPD-1 only had a moderate effect on tumor inhibition, which consolidated the therapeutic efficacy of MFC by on-demand O_2 production augmented sonodynamic immunotherapy. Survival analysis showed that 80% percent of mice exposed by MFC-reinforced SDT+aPD-1 survived to day 45, more than 2-fold higher than that of other groups (**Figure 6F**). Hematoxylin-eosin (H&E) and TdT-mediated dUTP nick-end labeling (TUNEL) staining of the tumor sections further revealed the most significant apoptosis and necrosis of tumors in the MFC+US+aPD-1 group (**Figure 6H**). Therefore, we reasonably believe that the on-demand O_2 production augmented sonodynamic therapy combined with immune checkpoint blockade was likely more efficient than traditional successive administration of sonodynamic immunotherapy.

Regarding safety, no noticeable weight or temperature changes were recorded throughout the observation period among the groups (**Figure 6G, Figure S18**). H&E staining of the major organs (including the heart, liver, spleen, lungs, and kidneys) revealed negligible toxicity among the six groups (**Figure S19**). The results indicated that the therapeutic dose in our work was well tolerated. The biocompatibility of the therapeutic process was further assessed in healthy Kunming mice by routine blood tests and blood biochemical analysis, and no obvious differences were observed among the groups at 21 days posttreatment (**Figure S20**). In addition, H&E staining of the major organs (including the heart, liver, spleen, lungs, and kidneys) displayed no obvious pathological damage or inflammatory lesions during our observation time (**Figure S21**). The ICP results showed that the MFC has a half-time time of 8.69 h, indicating the high biosafety of MFC with fast elimination capability in blood circulation (**Figure S22**). Overall, MFC showed remarkable antitumor effects with minimal systemic toxicity after sonodynamic immunotherapy.

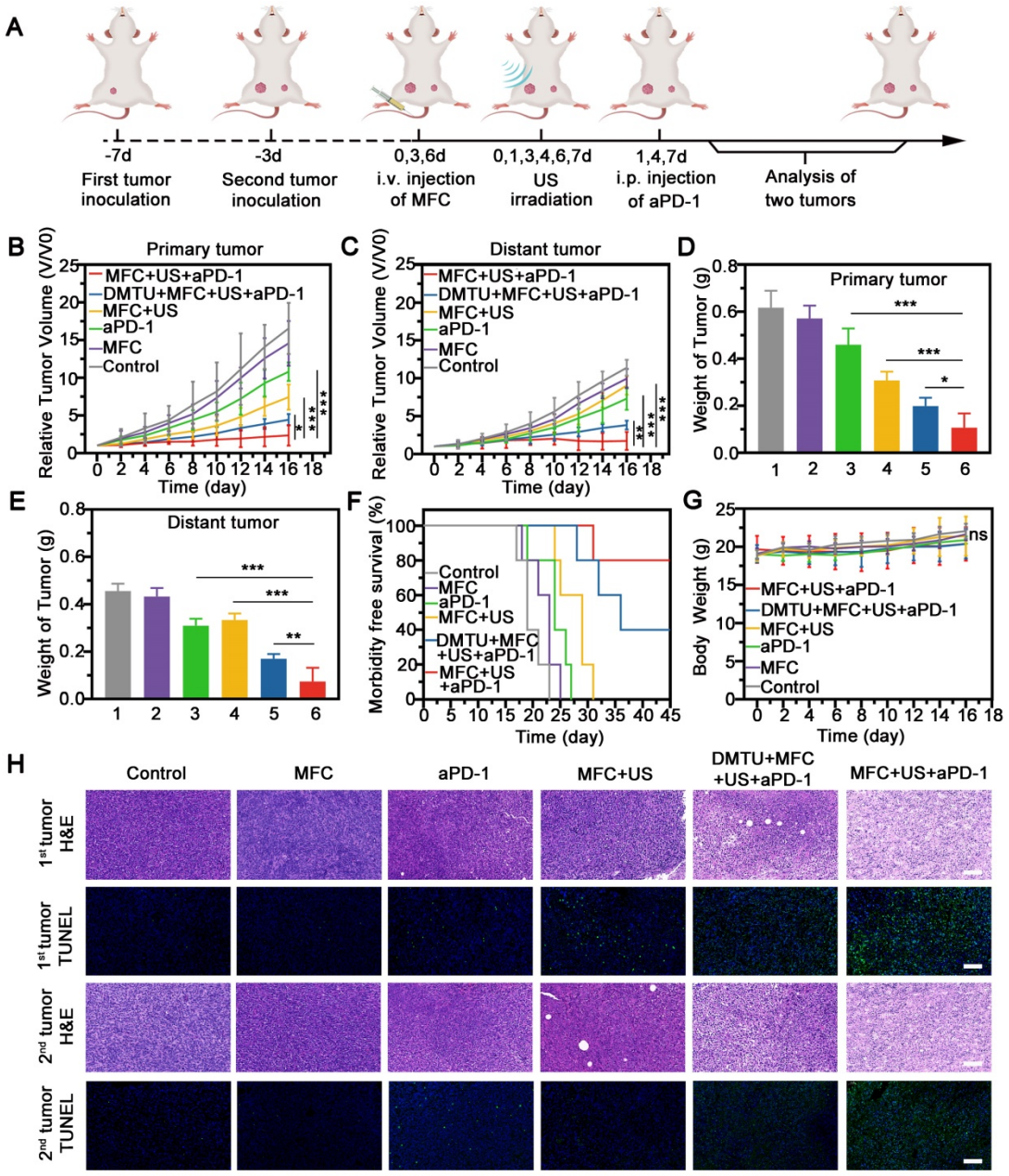

Figure 6. Therapeutic efficacy of MFC combined with aPD-1-mediated on-demand sonodynamic immunotherapy. (A) Schematic illustration of MFC-mediated SDT plus aPD-1 to suppress the growth of tumors at the primary or distant site in a tumor-bearing mouse model. (B-C) Growth curves of primary tumors and distant tumors. (D-E) Tumor weights of primary and distant tumors after different treatments.(1:Control, 2:MFC, 3:aPD-1, 4:MFC+US, 5:DMTU+MFC+US+ aPD-1, 6:MFC+US+aPD-1) (F) Morbidity-free survival of mice after various treatments. (G) Time-dependent body weight curves of the 4T1 tumor-bearing mice after different treatments. (H) H&E staining and TUNEL staining of primary and distant tumors. Scale bar: 100 μm.

Antitumor Immune Mechanisms

Sonodynamic therapy (SDT) can trigger immunogenic cell death (ICD) with release of tumor-associated antigens (TAAs). The released TAAs could facilitate the maturation of dendritic cells (DCs) in the tumor-draining lymph nodes and present TAAs to activate effector T cells. To explore the underlying mechanism of the tumor-specific immunological effect evoked by MFC+US+aPD-1, tumor-draining lymph nodes were harvested on the 8th day and analyzed by flow cytometry. The results showed MFC+US+aPD-1 could effectively elevate the percentage of mature DCs from 20.5% (Control) to 41.4% (MFC+US+aPD-1) (**Figure 7A-B**). Moreover, DMTU could significantly reduce the maturation of DCs, further indicating the importance of H_2O_2 in MFC-based sonodynamic immunotherapy.

$CD8^+$ T cells ($CD3^+CD4^-CD8^+$), known as CTLs, can kill tumor cells directly and are vital in the antitumor immune response.[49, 50] Therefore, $CD8^+$ T cell infiltration in distant tumors at the 8th day was examined by flow cytometry. The results showed that the percentage of $CD8^+$ T cells in the MFC+US+aPD-1

group was 49.4%, significantly increasing (by nearly 2.1-fold) compared to the control group (**Figure 7C-D**). Moreover, the proportion of $CD8^+$ T cells in the MFC+US+aPD-1 group was higher than those in both the MFC+US group and the aPD-1 group, indicating that the therapeutic outcome was markedly better than that of either SDT or immunotherapy alone. Moreover, DMTU could significantly reduce the infiltration of $CD8^+$ T cells, further indicating the importance of H_2O_2 in sonodynamic immunotherapy and the on-demand O_2 supply could enhance the efficacy of sonodynamic immunotherapy. Unlike $CD8^+$ T cells, regulatory T cells (Tregs, $CD4^+CD25^+Foxp3^+$) can protect tumor cells to avoid attack from the immune system and suppress the antitumor immune response.[51, 52] Therefore, the distant tumor was collected at the 8th day and costained with CD4, CD25, and Foxp3 for further analysis. The results showed that the percentage of Tregs in the MFC+US+aPD-1 group was much lower than that in the other groups (**Figure 7E-F**), demonstrating significant attenuation of the immunosuppressive environment of the tumor. Secreted cytokines, including tumor necrosis factor-α (TNF-α), interferon-γ (IFN-γ) and interleukin-6 (IL-6), are also important biomarkers that can indicate the potency of the immune response. Based on this, we further explored the levels of cytokines in distant tumors after various treatments on the 8th day. There was a significant increase in the production of TNF-α, IFN-γ, and IL-6 in the MFC+US+aPD-1 group compared to the control, monotherapy groups, and DMTU+MFC+US+aPD-1 group (**Figure 7G-7I**), verifying the strong antitumor immune potency induced by MFC-based SDT plus aPD-1. In addition, the infiltration of $CD8^+$ T cells into distant tumors was evaluated by immunofluorescence staining. As shown in **Figure 7j**, the infiltration of $CD8^+$ T cells was significantly increased in the MFC+US+aPD-1 group, indicating that MFC+US+aPD-1 could effectively recruit T cells to initiate a robust immune response.

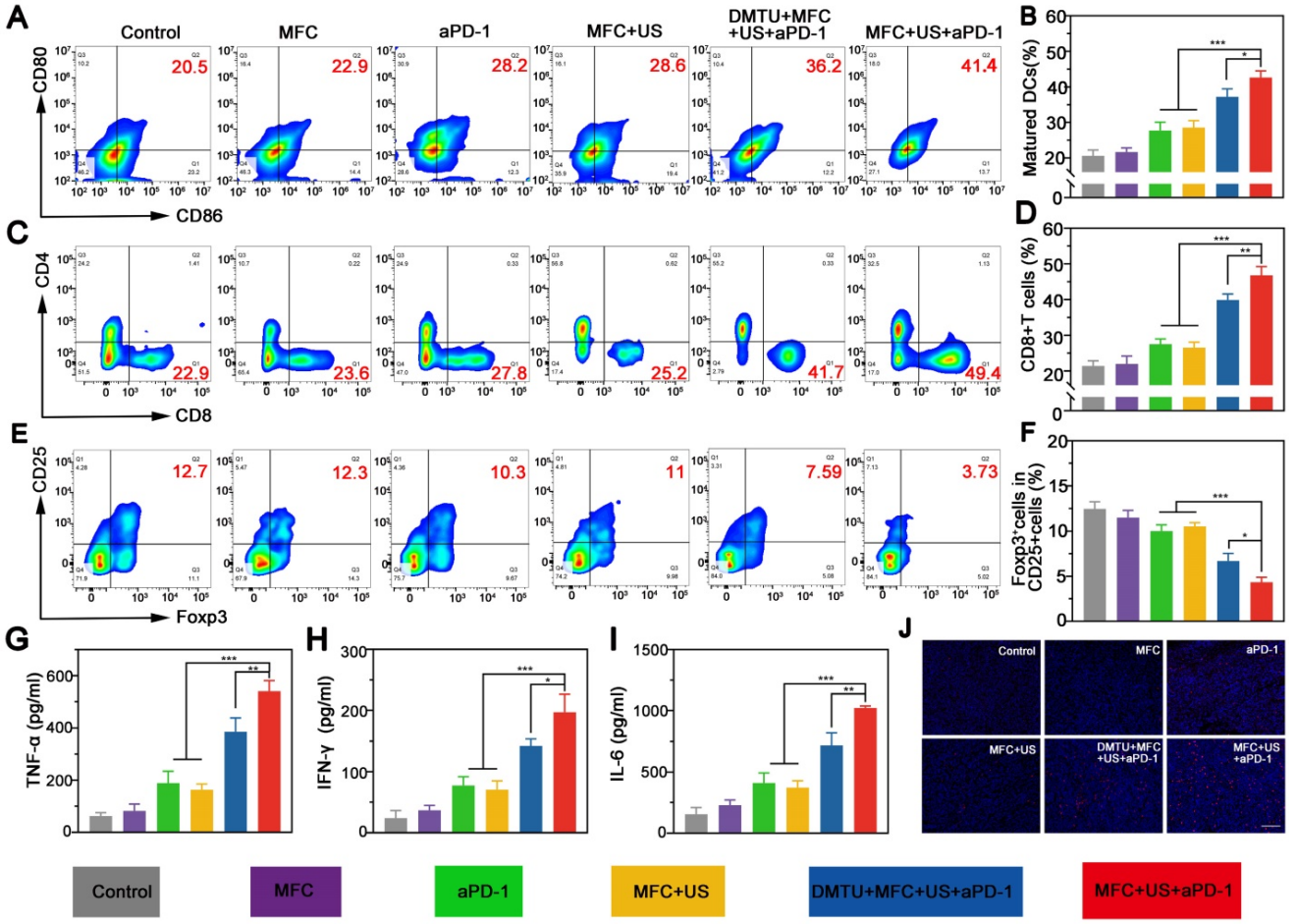

Figure 7. The immune mechanistic study. (A) Flow cytometry assay of matured DCs ($CD80^+$ $CD86^+$ gated on $CD11c^+$) in tumor-draining lymph nodes of mice after different treatments and (B) corresponding quantitative data. (C) Representative flow cytometry plots of $CD8^+$ T cells (gated on $CD3^+$ cells) and (D) corresponding quantitative data in distant tumors after different treatments. (E) Representative flow cytometry plots of Tregs ($CD4^+CD25^+Foxp3^+$) (gated on $CD4^+$ cells) (F) corresponding quantitative data in distant tumors after different treatments. (G,H,I) Cytokine levels in distant tumor tissues after different treatments. (J) Immunofluorescence staining of $CD8^+$ T cell infiltration in distant tumors after various treatments. Scale bar: 100 μm.

Conclusions

In conclusion, we developed the H_2O_2 economizer MFC to overcome the limitations of hypoxia in sonodynamic immunotherapy. By taking full advantage of the ultrasonic cavitation effect, we endowed MFC with US-responsive disintegration characteristics. The catalytic activity of Fe-PDAP was greatly reduced after attachments of Ce6 and cancer cell membranes, which successfully achieved on-demand O_2 production without the additional consumption of H_2O_2. By employing a biomimetic engineering strategy with cancer cell membranes, we addressed the premature leakage issue and increased tumor-site accumulation of MFC. We confirmed the hypoxia relief capability of MFC+US in tumor cells, while MFC alone could not efficiently alleviate tumor hypoxia. Upon US irradiation, the accumulated MFC disintegrated into Fe-PDAP to further improve tumor oxygenation in an on-demand manner. In addition, systemic administration of MFC+US combined with aPD-1 showed not only superior efficacy in combatting both primary, but also distant tumors. This study established a "broadening source of H_2O_2" strategy for the reversal of hypoxia during O_2-dependent sonodynamic immunotherapy. It also provided a strategy between O_2-enhanced sonodynamic therapy and immunotherapy for eradicating tumors.

Abbreviations

Fe-PDAP: Fe-doped polydiaminopyridine; SDT: Sonodynamic therapy; aPD-1: anti-programmed cell death protein-1 antibody; ROS: reactive oxygen species; ICD: immunogenic cell death; TAAs: tumor-associated antigens; TME: tumor microenvironment; H_2O_2: hydrogen peroxide; Ce6: chlorin e6; DCs: dendritic cells; TEM: transmission electron microscope; SEM: scanning electron microscope; PDI: polydispersity index; ICP-MS: inductively coupled plasma mass spectrometry; PMSF: phenylmethanesulfonyl fluoride; ESR: electron spin resonance; SOSG: singlet oxygen sensor green; CCK-8: cell counting kit-8; DMTU: 1, 3-Dimethylthiourea; CLSM: confocal laser scanning microscope; PAI: photoacoustic imaging; SDS-PAGE: sodium dodecyl sulfate-polyacrylamide gel electrophoresis; HE: hematoxylin & eosin; TUNEL: terminal deoxynucleotidyl transferase-mediated dUTP-biotin nick and labeling.

Supplementary Material

Supplementary figures.
https://www.thno.org/v12p0059s1.pdf

Acknowledgments

The authors are sincerely grateful for financial support from the Natural Science Foundation Project (81971633, 31630026, 81771847, 81971636), the project of China Postdoctoral Science Foundation (2021M690171), Venture & Innovation Support Program for Chongqing Overseas Returnees (cx2019027), the key project of Chongqing natural science Foundation (cstc2019jcyj-zdxmX0019), and the Key Project of Application Development Plan of Chongqing City (Grant No.cstc2019jscx-dxwtBX0004).

Competing Interests

The authors have declared that no competing interest exists.

References

1. Yue W, Chen L, Yu L, Zhou B, Yin H, Ren W, et al. Checkpoint blockade and nanosonosensitizer-augmented noninvasive sonodynamic therapy combination reduces tumour growth and metastases in mice. Nat Commun. 2019; 10: 2025.
2. Son S, Kim JH, Wang X, Zhang C, Yoon SA, Shin J, et al. Multifunctional sonosensitizers in sonodynamic cancer therapy. Chem Soc Rev. 2020; 49: 3244-61.
3. Liang S, Deng X, Ma P, Cheng Z, Lin J. Recent advances in nanomaterial-assisted combinational sonodynamic cancer therapy. Adv Mater. 2020; 32: e2003214.
4. Liang S, Xiao X, Bai L, Liu B, Yuan M, Ma P, et al. Conferring Ti-based MOFs with defects for enhanced sonodynamic cancer therapy. Adv Mater. 2021; 33: e2100333.
5. Yu W, Liu T, Zhang M, Wang Z, Ye J, Li CX, et al. O2 economizer for inhibiting cell respiration to combat the hypoxia obstacle in tumor treatments. ACS Nano. 2019; 13: 1784-94.
6. Phua SZF, Yang G, Lim WQ, Verma A, Chen H, Thanabalu T, et al. Catalase-integrated hyaluronic acid as nanocarriers for enhanced photodynamic therapy in solid tumor. ACS Nano. 2019; 13: 4742-51.
7. Yang J, Hou M, Sun W, Wu Q, Xu J, Xiong L, et al. Sequential PDT and PTT using dual-modal single-walled carbon nanohorns synergistically promote systemic immune responses against tumor metastasis and relapse. Adv Sci (Weinh). 2020; 7: 2001088.
8. Sheng D, Liu T, Deng L, Zhang L, Li X, Xu J, et al. Perfluorooctyl bromide & indocyanine green co-loaded nanoliposomes for enhanced multimodal imaging-guided phototherapy. Biomaterials. 2018; 165: 1-13.
9. Xia D, Hang D, Li Y, Jiang W, Zhu J, Ding Y, et al. Au-hemoglobin loaded platelet alleviating tumor hypoxia and enhancing the radiotherapy effect with low-dose X-ray. ACS Nano. 2020; 14: 15654-68.
10. Cheng Y, Cheng H, Jiang C, Qiu X, Wang K, Huan W, et al. Perfluorocarbon nanoparticles enhance reactive oxygen levels and tumour growth inhibition in photodynamic therapy. Nat Commun. 2015; 6: 8785.
11. Qiao Y, Yang F, Xie T, Du Z, Zhong D, Qi Y, et al. Engineered algae: A novel oxygen-generating system for effective treatment of hypoxic cancer. Sci Adv. 2020; 6: eaba5996.
12. Li Y, Sun P, Zhao L, Yan X, Ng DKP, Lo PC. Ferric ion driven assembly of catalase-like supramolecular photosensitizing nanozymes for combating hypoxic tumors. Angew Chem Int Ed Engl. 2020.
13. Sun D, Pang X, Cheng Y, Ming J, Xiang S, Zhang C, et al. Ultrasound-switchable nanozyme augments sonodynamic therapy against multidrug-resistant bacterial infection. ACS Nano. 2020; 14: 2063-76.
14. Yang G, Xu L, Chao Y, Xu J, Sun X, Wu Y, et al. Hollow MnO2 as a tumor-microenvironment-responsive biodegradable nano-platform for combination therapy favoring antitumor immune responses. Nat Commun. 2017; 8: 902.
15. Liu CP, Wu TH, Liu CY, Chen KC, Chen YX, Chen GS, et al. Self-Supplying O2 through the catalase-like activity of Gold nanoclusters for photodynamic therapy against hypoxic cancer cells. Small. 2017; 13.
16. Bao Y, Chen J, Qiu H, Zhang C, Huang P, Mao Z, et al. Erythrocyte membrane-camouflaged PCN-224 nanocarriers integrated with platinum nanoparticles and glucose oxidase for enhanced tumor sonodynamic therapy and synergistic starvation therapy. ACS Appl Mater Interfaces. 2021; 13: 24532-42.
17. Chen J, Bao Y, Song Y, Zhang C, Qiu F, Sun Y, et al. Hypoxia-alleviated nanoplatform to enhance chemosensitivity and sonodynamic effect in pancreatic cancer. Cancer Lett. 2021; 520: 100-8.
18. Ding M, Miao Z, Zhang F, Liu J, Shuai X, Zha Z, et al. Catalytic rhodium (Rh)-based (mesoporous polydopamine) MPDA nanoparticles with enhanced

phototherapeutic efficiency for overcoming tumor hypoxia. Biomater Sci. 2020; 8: 4157-65.
19. Tang W, Yang Z, He L, Deng L, Fathi P, Zhu S, et al. A hybrid semiconducting organosilica-based O2 nanoeconomizer for on-demand synergistic photothermally boosted radiotherapy. Nat Commun. 2021; 12: 523.
20. Yang B, Chen Y, Shi J. Reactive oxygen species (ROS)-based nanomedicine. Chem Rev. 2019; 119: 4881-985.
21. Song M, Cheng Y, Tian Y, Chu C, Zhang C, Lu Z, et al. Sonoactivated chemodynamic therapy: A robust ROS generation nanotheranostic eradicates multidrug-resistant bacterial infection. Adv Func Mater; 2020; 30: 2003587.
22. Qiao B, Luo Y, Cheng HB, Ren J, Cao J, Yang C, et al. Artificial nanotargeted cells with stable photothermal performance for multimodal imaging-guided tumor-specific therapy. ACS Nano. 2020; 14: 12652-67.
23. Rezk AR, Ahmed H, Ramesan S, Yeo LY. High frequency sonoprocessing: A new field of cavitation-free acoustic materials synthesis, processing, and manipulation. Adv Sci (Weinh). 2020; 8: 2001983.
24. Ho YJ, Li JP, Fan CH, Liu HL, Yeh CK. Ultrasound in tumor immunotherapy: Current status and future developments. J Control Release. 2020; 323: 12-23.
25. Qian X, Zheng Y, Chen Y. Micro/nanoparticle-augmented sonodynamic therapy (SDT): breaking the depth shallow of photoactivation. Adv Mater. 2016; 28: 8097-129.
26. Nanzai B, Suzuki S, Okitsu K. Sonochemical degradation of surfactants with different charge types: Effect of the critical micelle concentration in the interfacial region of the cavity. Ultrason Sonochem. 2021; 71: 105354.
27. Huo S, Zhao P, Shi Z, Zou M, Yang X, Warszawik E, et al. Mechanochemical bond scission for the activation of drugs. Nat Chem. 2021; 13: 131-9.
28. Ma Y, Zhao Y, Bejjanki NK, Tang X, Jiang W, Dou J, et al. Nanoclustered cascaded enzymes for targeted tumor starvation and deoxygenation-activated chemotherapy without systemic toxicity. ACS Nano. 2019; 13: 8890-902.
29. Fan JX, Peng MY, Wang H, Zheng HR, Liu ZL, Li CX, et al. Engineered bacterial bioreactor for tumor therapy via fenton-like reaction with localized H2O2 generation. Adv Mater. 2019; 31: e1808278.
30. Wang S, Yu G, Wang Z, Jacobson O, Lin LS, Yang W, et al. Enhanced antitumor efficacy by a cascade of reactive oxygen species generation and drug release. Angew Chem Int Ed Engl. 2019; 58: 14758-63.
31. Xiao J, Zhang G, Xu R, Chen H, Wang H, Tian G, et al. A pH-responsive platform combining chemodynamic therapy with limotherapy for simultaneous bioimaging and synergistic cancer therapy. Biomaterials. 2019; 216: 119254.
32. Dai Y, Yang Z, Cheng S, Wang Z, Zhang R, Zhu G, et al. Toxic reactive oxygen species enhanced synergistic combination therapy by self-assembled metal-phenolic network Nanoparticles. Adv Mater. 2018; 30.
33. Pan X, Bai L, Wang H, Wu Q, Wang H, Liu S, et al. Metal-organic-framework-derived carbon nanostructure augmented sonodynamic cancer therapy. Adv Mater. 2018; 30: e1800180.
34. Zhu L, Zhao H, Zhou Z, Xia Y, Wang Z, Ran H, et al. Peptide-functionalized phase-transformation nanoparticles for low intensity focused ultrasound-assisted tumor imaging and therapy. Nano Lett. 2018; 18: 1831-41.
35. Zhong Y, Zhang Y, Xu J, Zhou J, Liu J, Ye M, et al. Low-intensity focused ultrasound-responsive phase-transitional nanoparticles for thrombolysis without vascular damage: A synergistic nonpharmaceutical strategy. ACS Nano. 2019; 13: 3387-403.
36. Rao L, Bu LL, Cai B, Xu JH, Li A, Zhang WF, et al. Cancer cell membrane-coated upconversion nanoprobes for highly specific tumor imaging. Adv Mater. 2016; 28: 3460-6.
37. Hu CM, Fang RH, Wang KC, Luk BT, Thamphiwatana S, Dehaini D, et al. Nanoparticle biointerfacing by platelet membrane cloaking. Nature. 2015; 526: 118-21.
38. Shao D, Li M, Wang Z, Zheng X, Lao YH, Chang Z, et al. Bioinspired diselenide-bridged mesoporous silica nanoparticles for dual-responsive protein delivery. Adv Mater. 2018: e1801198.
39. Zhen X, Cheng P, Pu K. Recent advances in cell membrane-camouflaged nanoparticles for cancer phototherapy. Small. 2019; 15: e1804105.
40. Bai J, Jia X, Zhen W, Cheng W, Jiang X. A Facile ion-doping strategy To regulate tumor microenvironments for enhanced multimodal tumor theranostics. J Am Chem Soc. 2018; 140: 106-9.
41. Zhao G, Liu T, Wu B, Chen B, Chu C. Constructing the support as a microreactor and regenerator for highly active and *in situ* regenerative hydrogenation catalyst. n/a: 2100971.
42. Shchukin DG, Gorin DA, Mohwald H. Ultrasonically induced opening of polyelectrolyte microcontainers. Langmuir. 2006; 22: 7400-4.
43. Wen M, Ouyang J, Wei C, Li H, Chen W, Liu YN. Artificial enzyme catalyzed cascade reactions: Antitumor immunotherapy reinforced by NIR-II light. Angew Chem Int Ed Engl. 2019; 58: 17425-32.
44. Kim SH, Kim B, Yadavalli VK, Pishko MV. Encapsulation of enzymes within polymer spheres to create optical nanosensors for oxidative stress. Anal Chem. 2005; 77: 6828-33.
45. Cao J, Qiao B, Luo Y, Cheng C, Yang A, Wang M, et al. A multimodal imaging-guided nanoreactor for cooperative combination of tumor starvation and multiple mechanism-enhanced mild temperature phototherapy. Biomater Sci. 2020; 8: 6561-78.
46. Liu F, Lin L, Zhang Y, Wang Y, Sheng S, Xu C, et al. A tumor-microenvironment-activated nanozyme-mediated theranostic nanoreactor for imaging-guided combined tumor therapy. Adv Mater. 2019; 31: e1902885.
47. Luo Y, Qiao B, Zhang P, Yang C, Cao J, Yuan X, et al. TME-activatable theranostic nanoplatform with ATP burning capability for tumor sensitization and synergistic therapy. Theranostics. 2020; 10: 6987-7001.
48. Xiang Q, Qiao B, Luo Y, Cao J, Fan K, Hu X, et al. Increased photodynamic therapy sensitization in tumors using a nitric oxide-based nanoplatform with ATP-production blocking capability. Theranostics. 2021; 11: 1953-69.
49. Huang L, Li Y, Du Y, Zhang Y, Wang X, Ding Y, et al. Mild photothermal therapy potentiates anti-PD-L1 treatment for immunologically cold tumors via an all-in-one and all-in-control strategy. Nat Commun. 2019; 10: 4871.
50. Chen Q, Chen J, Yang Z, Xu J, Xu L, Liang C, et al. Nanoparticle-enhanced radiotherapy to trigger robust cancer immunotherapy. Adv Mater. 2019; 31: e1802228.
51. Zou W. Regulatory T cells, tumour immunity and immunotherapy. Nat Rev Immunol. 2006; 6: 295-307.
52. Byrne A, Savas P, Sant S, Li R, Virassamy B, Luen SJ, et al. Tissue-resident memory T cells in breast cancer control and immunotherapy responses. Nat Rev Clin Oncol. 2020; 17: 341-8.